Performance limitations and analysis of silicon heterojunction solar cells using very thin MoO_x hole-selective contacts

J. Dréon, J. Cattin, G. Christmann, D. Fébba, V. Paratte, L. Antognini, W. Lin, S. Nicolay, C. Ballif, M. Boccard

***Abstract* — We recently showed that silicon heterojunction solar cell with MoO_x-based hole-selective contact could reach 23.5% in efficiency with MoO_x layers of 4 nm. Such thin MoO_x layer enables a considerable current-density gain of over 1 mA/cm^2 compared to the use of p-type amorphous silicon, and outperforms thicker MoO_x layers. In this study, we investigated the impact of the MoO_x hole-selective layer for thickness between 0 and 4 nm. Based on opto-electrical characterization of the device at various processing stage, we discuss the optical and electrical effects of such variation on the solar-cell performances. We notably identify a loss of passivation and selectivity for MoO_x films thinner than 4 nm, that we link to a reduced work-function for such thin MoO_x films. We confirm experimentally that the optimal MoO_x thickness is around 4 nm, yet evidence that close to 0.5 mA/cm^2 is still parasitically absorbed in such a thin layer.**

***Index Terms*— Solar cells, silicon heterojunction, metal-oxides, molybdenum oxide, selectivity, passivation, passivating contact.**

I. Introduction

SILICON heterojunctions (SHJ) solar cells using hydrogenated-amorphous-silicon (a-Si:H) passivating contacts are known for simple processing combined with high efficiencies [1], [2]. Yet, their performances are hindered by parasitic absorption in the a-Si:H layers, with current losses up to 2.8 mA/cm^2 from p-type (p)a-Si:H and 1.9 mA/cm^2 from intrisinc (i)a-Si:H [3]–[5]. In the pursuit of current-loss mitigation, many wide-bandgap silicon-based materials such as (n)μc-Si (micro-crystalline Si) [6], (n)nc-SiO_x:H (nano-crystalline SiO_x) or (p)uc-SiOx:H [7][8], SiOx/(p)μc-Si [9], SiO_x/(n)μc-Si:C [10] or (p)nc-Si:H/(p)nc-SiOx:H [11] stacks have been developed to replace a-Si:H. New Si-free materials are promising alternatives to Si-based contacts, due to the wide amount of available compounds and unlimited tunable properties to investigate. Integrated in solar cells, they have already proved high performances, like with PEDOT:PSS [12][13], TiN_x [14], b-PEI/Al [15], TiOx/LiF_x/Al [16], ZnO/LiF_x/Al [17] or MgF_x/Mg/Al [18], mostly used as rear contact, and WO_3, V_2O_5 [19] or NiOx [20], [21] to replace front hole contact. Si-free contacts replacing both holes and electron contacts with different architectures, such as bifacial [22] or interdigitated back contacted (IBC) [18] solar cells, have also been developed.

Sub-stoichiometric molybdenum trioxide (MoO_x) stands so far as the most successful non-silicon-based approach to replace the p-doped hydrogenated amorphous silicon (p)a-Si:H front hole selective layer (see Fig. 1) [18], [23]–[26]. In a previous work [26], we demonstrated that thinning down the MoO_x front hole selective layer from 9 nm to 4 nm (in this work, all thicknesses are given on textured surfaces, calculated from measurements on flat Si or glass divided by a ratio of 1.6 accounting for the pyramids geometry [27]) significantly improved photocurrent while maintaining excellent hole-selectivity and front surface passivation, enabling high operating voltages. As a result, we demonstrated a 23.5% efficient 4-nm-MoO_x-based heterojunction solar cell, notably thanks to a photocurrent 1.3 mA.cm^{-2} higher than the reference

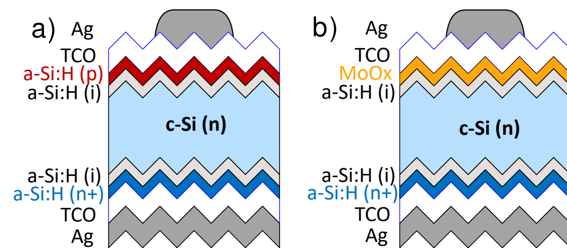

Fig. 1. Scheme of a silicon heterojunction solar cell, with a hole contact a) based on a-Si:H (standard), and b) MoO_x-based

device using (p)a-Si:H as hole selective layer. However, the best efficiency of the series was obtained for the thinnest tested layer, intimating that the optimum may not be reached yet. Extrapolating the current-density trends observed between 9-nm- and 4-nm-thick MoO_x films to a 1-nm-thick MoO_x layer

Manuscript received January xx, 2021. This project has received funding from the Swiss national science foundation under Ambizione Energy grant ICONS (PZENP2_173627) as well as under the grant no. 200021L_172924/1.

J. Dréon, J. Cattin, D. Febba, V. Paratte, L. Antognini, W. Lin, C. Ballif, and M. Boccard are with the École Polytechnique Fédérale de Lausanne (EPFL), Institute of Microengineering (IMT), Photovoltaics and Thin Film Electronics Laboratory, Rue de la Maladière 71b, CH-2002 Neuchâtel, Switzerland (corresponding author: +41 21 695 42 64; e-mail: julie.dreon@epfl.ch).

G. Christmann, S. Nicolay and C. Ballif are with the Centre Suisse d'Electronique et de Microtechnique SA (CSEM), Rue Jaquet-Droz 1,2002 Neuchâtel, Switzerland.

W. Lin is with Institute for Solar Energy Systems, Guangdong Provincial Key Laboratory of Photovoltaic Technology, School of Physics and State Key Laboratory of Optoelectronic Materials and Technologies, Sun Yat-Sen University, Guangzhou 510006, China.

D. Febba is with Universidade Federal de Itajubá, Av. B P S, 1303 - Pinheirinho, Itajubá - MG, 37500-903, Brazil. His work was sponsored by the National Council for Scientific and Technological Development (CNPq - Brazil) and by the Federal Commission for Scholarships for Foreign Students (FCS - Switzerland) in the form of scholarships.

suggested a possible current density gain of another 0.75 mA/cm^2. We investigate thus here if thinning down the MoO_x layer below 4 nm indeed enables this current-density gain. Furthermore, we explore in detail how MoO_x thickness lower than 4 nm influences selectivity and passivation of devices using MoO_x as a hole-selective layer.

II. Experimental Details

Five silicon heterojunction samples each consisting of five cells were fabricated following the same process sequence as described in [28], variating MoO_x thickness between 0 nm (no MoO_x layer) and 4 nm[1]. We used 195-µm-thick n-type textured float zone wafers with a resistivity of 1.7-2.3 Ωcm. A stack composed of amorphous and microcrystalline (µc) hydrogenated silicon, (i)a-Si:H/(n)a-Si:H /(n)µc-Si:H, was deposited at the back side by plasma enhanced chemical vapor deposition (PECVD) at 200 °C on all wafers. A layer of 6 nm of (i)a-Si:H was then deposited on the front side of the wafers. After removal of the surface oxide in an aqueous solution of 5% diluted hydrofluoridric acid (HF), a 4-nm-, 3-nm- 2-nm- or 1-nm-thick MoO_x layer was thermally evaporated on the front side, while one sample did not receive MoO_x (neither (p)a-Si:H layer). MoO_x evaporation was done in a vacuum chamber (base pressure before deposition ~ 4×10^{-6} mbar) from stoichiometric MoO_3 powder at a deposition rate of about 0.03 nm/s. Finally, indium tin oxide (ITO, 70 nm) was sputtered on the front through a mask to form the five 2 x 2 cm^2 devices per wafer. ITO (150 nm) and Ag (100 nm) were then sputtered over the full back side area. A silver grid was finally screen-printed on the front side using a low-temperature paste, cured at 130 °C in a belt furnace. Fig. 2 summurizes the process flow.

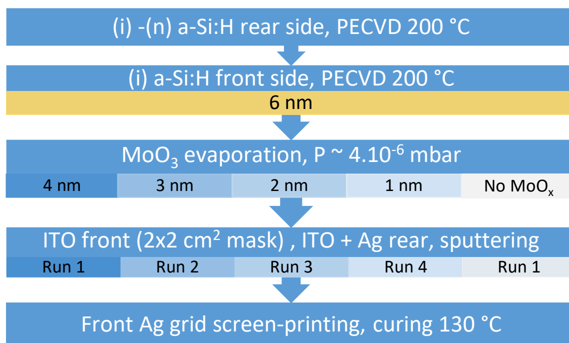

Fig. 2: Process flow of the different solar cells

The *J-V* characterization is performed with a Wacom WXS-90S-L2 solar simulator, under standard test condition (AM 1.5G, 100 mW/cm^2 at 25 °C). The cells are measured one by one, on the wafer through a mask hiding their edges and the rest of the wafer. The light spectrum intensity is calibrated every week through reference solar cell, over 315-800 nm, 650-1180 nm, and 315-1180 nm. Before each measurement, a reference solar cell is also used to adjust the calibration and normalize the current accordingly.

The external and internal quantum efficiency (EQE and IQE respectively) measurements are made utilizing in-house built setup, with a rectangular illumination beam which is 2 mm x 1 mm large. The measurement does not include finger shading, leading to a higher integrated current value compared to the one measured in J-V characterization. Lifetime measurements are performed with a Sinton Instrument WCT-120 by photoconductance decay in transient mode [29], [30]. For each wafer, measurement is performed at the five different solar cell location then averaged. Suns-Voc characterization are realized with a Sinton Instrument WCT-120 with an Illumination-Voltage tester stage.

III. Short-Circuit Current Density and Optics Analysis

Fig. 3.a) shows the IQE of all MoO_x-based cells in addition to a standard SHJ cell reference processed in the same week, and Table 1 summarizes the MoO_x-based cells short-circuit current density (J_{SC}) gain compared to this reference.

The 4 nm-thick MoO_x sample has a gain identical to the one

TABLE I

MoOx thickness (nm)	Total MoO_x-based cells J_{SC} gain compared to standard SHJ (mA/cm^2)
4	1.35
3	1.42
2	1.81
1	1.88
0	.72

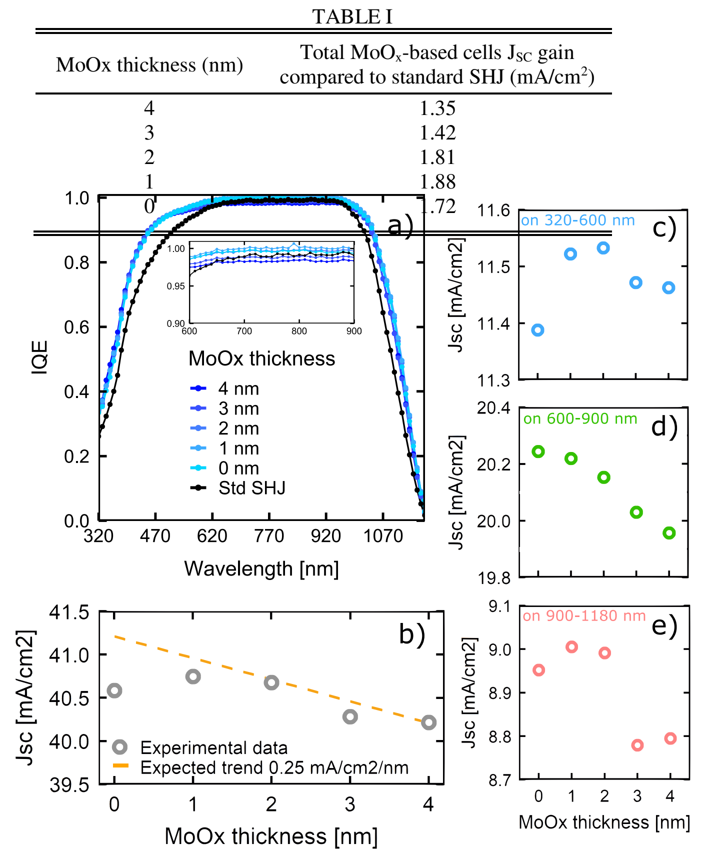

obtained in the previous experiment, confirming the robustness of this metric. J_{SC} is increasing with thinner MoO_x-layer samples, from 4-nm to 1-nm-thick MoO_x. This increase partially originates from the reduced MoO_x sub-bandgap parasitic absorption which occurs on the range 600 nm – 900 nm [28], as shown by the zoomed in plot on Fig. 3.a). It is completely evicted for devices with a MoO_x layer thickness strictly below 3 nm since their IQE values on this range are above the ones of the reference SHJ cell. This demonstrates that there is still parasitic absorption even in an optimal MoO_x layer

Fig. 3: a) IQE plots of the six different cells; b) current density evolution with MoO_x thickness; c) d) e): the different spectral contribution to current density against MoO_x thickness.

as thin as 4 nm, amounting to ~ (0.5)~~1.0~~ mA/cm^2. The trend reverses from 1 nm to 0 nm thick MoO_x and this is also highlighted on Fig 3.b, where experimental J_{SC} extracted from EQE for all samples are plotted together with the expected trend of 0.25 mA/cm^2/nm (calculated from our previous work with MoO_x layer thinned from 9 nm to 4 nm). To identify the origin of this deviation, the J_{SC} contribution from three spectrum regions (320-600 nm, 600-900 nm, and 900-1180 nm) are displayed in Fig. 3.c), d) and e). The J_{SC} departure from the expected trend mostly originates from the wavelength range 320-600 nm (see Fig. 3 c)) and affects both the 0-nm and 1-nm-thick MoO_x samples. On one hand, thinning down the ITO/MoO_x-stack thickness is expected to shift the minimum of reflection to shorter wavelengths, thus to increase the EQE response in this range. On the other hand, a drop in front passivation would reduce at a point the J_{SC}, especially this short-wavelength range, since high front recombination will interfere with charge extraction. These two effects were simulated using PC1D to evaluate their expected magnitude. Thinning down the antireflective coating (ARC) by 4 nm increases J_{SC} on the 320-600 nm range by 0.4 mA/cm^2, which is opposite to the observed deviation.

Conversely, increasing the front-surface recombination velocity from 10 cm/s (simulating a well-passivated surface for SHJ) to 10^7 cm/s (corresponding to a very poor surface passivation) resulted in a J_{SC} loss of 0.4 mA/cm^2 on this same wavelength range, which is consistent with the observed deviation. Although simplistic, these qualitative simulations correspond to the same order of magnitude of J_{SC} variation as the one we observed in our experiment, and suggest that the observed J_{SC} loss when using a too thin MoO_x film can be attributed to passivation damage, which will be discussed in the following.

The small J_{SC} loss for the 0-nm-thick MoO_x sample on the range 900-1180 nm (Fig. 3.e)) can be attributed to the aforementioned effect of minimum of reflection shift towards shorter wavelengths. An oxygen exchange from MoO_x to ITO, decreasing the doping of the latter, would also mitigate the free carrier absorption responsible for parasitic absorption in the near infrared (IR) range and

enhance the MoO_x-based cells IR response in comparison with no MoO_x-based layers.

IV. Electrical Analysis

The extracted *J-V* electrical parameters of the five devices (open circuit voltage (V_{OC}), J_{SC}, fill factor (*FF*), efficiency (Eff.)) are plotted in shades of blue in Fig. 4.a), b), c), d) respectively. In addition, data from the previous experiment (same process steps but MoO_x thickness from 9 to 4 nm) are displayed with pink shades on the same graph [28]. Globally, the 4-nm-thick MoO_x-based device of this new study has poorer performances (lower J_{SC} and *FF*) compared to the previous processed one, which can be explained by two aspects. First, the lower *FF* and slightly lower V_{OC} originate from a poorer passivation from the very beginning in the process steps (see Fig. 5), due to slight mechanical damage during the cleaning process, as well as possible wafer-quality variability or (i)a-Si:H batch-to-batch variability. *FF* is also slightly impacted by higher series resistance due to screen-printing issue for the front grid metallization. Nevertheless, the device employing a 4-nm-thick MoO_x layer exhibits globally good performances compared to the thinner-MoO_x devices.

From devices employing 9-nm-thick to 4-nm-thick MoO_x films, V_{oc} upholds above 700 mV whereas it drops from the 3-nm-

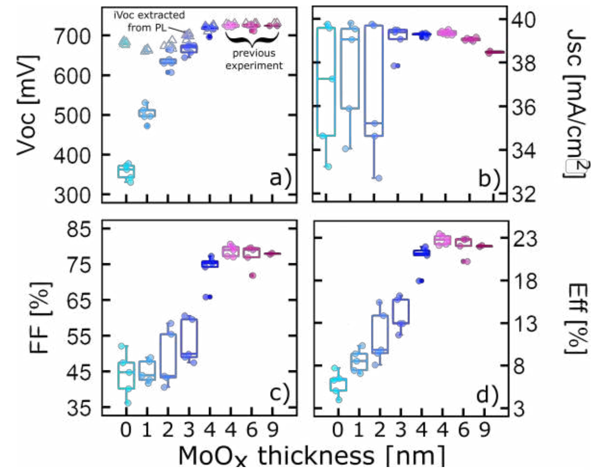

Fig. 4: a) b) c) d): electrical parameters extracted from the *J-V* characteristics of the solar cells processed in this work and previous one [8]. The iVoc values on graph a) are extracted from photoluminescence imaging on final solar cells structures (see below).

thick to 0-nm-thick MoO_x-based samples, with an increasingly steep slope. The same behavior is observed for *FF*, with an even more drastic drop. To identify the influence of passivation and selectivity on these losses, we performed lifetime measurements, photoluminescence (PL) imaging, suns-Voc at high illumination, and *J-V* curve fittings.

A. *Lifetime-base passivation investigation*

Fig. 5 shows the lifetime of the different samples after each process step, measured at a carrier injection of 5×10^{15} cm^{-3} which is around the range of solar cells standard operating carrier densities). The measurement after ITO front deposition is done prior to the screen the printing and annealing of the contacts. Here again, data from the previous experiment is

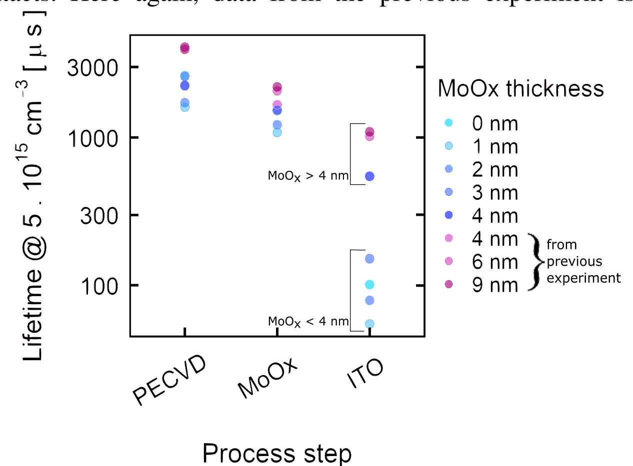

Fig. 5: Evolution of cells lifetime, taken at a carrier injection of 5×10^{15} /cm^3, through the different process steps

added (pink shades). Highest-lifetime samples after PECVD remain the best after MoO_x deposition, however an overall lifetime decrease is seen for all the samples after MoO_x deposition. Such drop is common after deposition of hole-selective contacts (including (p)a-Si:H layers), and is attributed to the shift of the Fermi level in the (i)a-Si:H layer towards the valence band edge [31], [32]. After the ITO front sputtering, all samples experience a lifetime decrease, attributed to sputtering damage (the measurement was done prior to any curing), but devices from 9-nm-thick to 4-nm-thick in both experiments hold a lifetime around 1 ms whereas the lifetime of the devices with thinner MoO_x films plunge down to 0.01-0.2 ms. Interestingly, the device with bare (i)a-Si:H maintains a lifetime superior to the devices having an additional 1-nm- or 2-nm-thick MoO_x layer. This could be due to the higher initial lifetime, or to a stronger impact of the sputter-damage when a very thin MoO_x film is present, presumably due to the aforementioned shifting of the Fermi-level closer to the valence band.

PL imaging of Fig. 6 gives a qualitative information about lifetime in the final device structure (the full area silver sputtering at the backside makes lifetime measurement by photoconductance decay impossible) after curing at 130 °C. It pictures the wafer with an injection equivalent to open circuit (OC) condition at one Sun. The PL intensity (arbitrary unit) is directly proportional to the radiative recombination rate, itself proportional to the $n \times p$ (n being the electrons concentration, p the holes one). Here, PL images were normalized to a common scale. The five solar cells per wafer appear as squares, corresponding to the ITO-pad area. Around these squares, ITO is not present, but those surfaces still received the MoO_x/(i)a-Si:H deposition. Scratches are visible on several images due to previously discussed mechanical damage during processing. The signal intensity for the 4-nm-thick MoO_x-based solar cells (with ITO) remains almost as high or half high as the signal intensity around these cells (no ITO), whereas the contrast between the solar cells (low response) and their surrounding (high response) for devices which received less than 4-nm-thick MoO_x is much stronger. The MoO_x being too thin, it may not protect the (i)a-Si:H layer enough, irreversibly damaging the cell surface passivation even after curing. For a more quantitative analysis, we extracted the implied open circuit voltage iV_{OC} from our PL images, which can be deduced from the $n \times p$ product [33], [34]. We calibrated the proportionality coefficient between the PL counts and $n \times p$ by assuming that the lifetime in the areas not covered by ITO is similar to the lifetime prior to ITO deposition. We thus used the iV_{OC} measured by photoconductance decay prior to ITO and Ag deposition as corresponding to the PL counts around the squared ITO-covered cells. The small differences in the front contact stack between samples are not expected to impact significantly the PL counts with respect to the passivation losses we observe.

Fig. 4.a) shows the iV_{OC} of the final devices. It drops by around 70 mV between the 4-nm-MoO_x sample and the 1-nm-MoO_x sample, vouching for the expected passivation loss. Nevertheless, the difference between the measured external V_{OC} of the devices and their iV_{OC} (noted ΔV_{OC}=iV_{OC}-V_{OC}) increases when thinning down the MoO_x layer, witnessing at a selectivity loss as well, in line with work from Bivour *et al.* [35].

B. Selectivity probing

In light of the previous result, we probed the selectivity of our front hole contact for all the different MoO_x layers thicknesses, through measurements and simulations.

1) Suns-V_{OC} measurements for recombination mechanism investigation and first selectivity study approach

We plotted illumination versus V_{OC}, also called "Suns-V_{OC}" analysis [30], [36], [37], of our best cell for each condition, from low (0.01 Suns) to high (135 Suns) illumination. In previous works, this kind of measurement at high illumination was demonstrated to highlight transport issues that can impact the cell selectivity, passivation and transport at one sun, [35], [37]. Notably, a deviation from the logarithmic V_{OC} increase with illumination was shown to be a signature of poorly selective hole contacts originating from the formation of a Schottky barrier due to work function misalignment. As depicted in Fig. 8, instead of stronger reversal in the curve appearing earlier and earlier as the MoO_x layer is thinned down from 4 to 0 nm, like it was observed in [35] and [37] for cells with weaker contact quality, we noticed no difference in our cells response at high illumination. It hints that there is no reverse Schottky diode impeding carrier extraction, even for the thinnest MoO_x layers. The green dashed and red dotted linear slopes are added to the plot as guide for the eyes, and

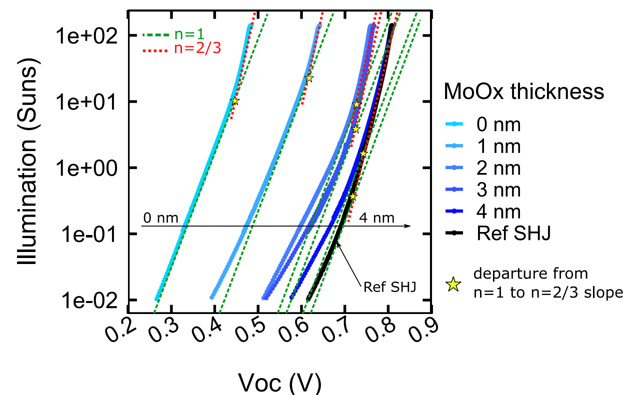

Fig. 8: Suns-V_{OC} measurements of the different cells, on a wide illumination range (0.01 to 135 Suns)

correspond to the response of an ideal p-n junction case with an ideality factor of n = 1 and n = 2/3 respectively, following the

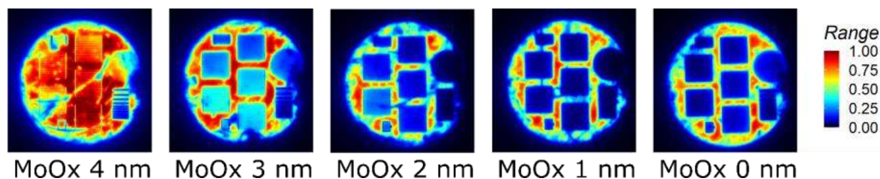

Fig. 6: PL imaging of the different cells, in open circuit conditions (1 Sun)

Shockley diode equation: $J(V) = J_0\left(e^{\frac{qV}{nkT}} - 1\right)$. The case n=1 corresponds to the ideal diode case with radiative recombination only and no traps involved in the processes [38], [39]. The case n=2/3 stands for a diode where Auger recombination is predominant [38], [40]. Globally, from 0.5 to 100 suns, all the cells follow these two regimes, switching from n=1 to n=2/3 at different illuminations according to the different MoO_x thicknesses. The cell with 4 nm of MoO_x works in high injection at an illumination a bit higher than 1 sun already (it changes regime from n=1 to n=2/3 at that illumination), which is typical of silicon heterojunction solar cells with good working contacts, whereas the cell with only 1 nm of MoO_x only reaches Auger regime around 20-sun illumination. This correlates well with the lifetime variations reported in Fig. 6 and 7, with higher-lifetime samples reaching Auger regime at lower illumination.

At lower illuminations (below 0.1 sun), so lower carrier injection, MoO_x-based cells show an ideality factor between 1 and 2, in general attributed to Shockley Read Hall recombination involving traps in the transport and recombination process [38], [39], [41]. Interestingly and contrary to the other samples, the cell without MoO_x (0 nm MoO_x) keeps an ideality factor of n=1 with a straight slope sticking to the ideal diode behavior. The same behavior is measured on a reference standard SHJ in a lower extent (see Fig. 8). This effect is unlikely linked to shunt resistance - which was not considered in the calculation-, since the calculation from dark *J-V* curves showed they were all above 1×10^5 Ωcm². It could either come from inhomogeneity of the MoO_x layer or even local pin-holes in this layer [42], or from a drop of passivation in low injection due to defects in a-Si:H following the shift of Fermi level closer to the valence band [31], [32]. These Suns-V_{OC} measurements show that sub-optimal MoO_x thickness has a fundamentally different influence on selectivity compared to too-lightly doped (p)a-Si:H [35].

2) *J_{0s} fitting through Roe et al. modeling*

To further understand the origin of the selectivity loss - and somehow the V_{OC} and *FF* drop – of our thin-MoO_x contacts, we fitted our *J-V* curves with the model of Roe *et al.* [43] which is adapted for contact-limited devices and relies on four partial currents (one for electrons and one for holes at each contact) as described in Fig. 9a. The current-voltage curve can be derived following equation (1), where J_L is the photogenerated density current, V_T the thermal voltage (k_BT/q, k_B the Boltzmann constant, T the temperature and q the electronic charge). J_{0h}^{MoOx} and j_{0e}^{MoOx} stand for the hole and electron equilibrium exchange current densities at the hole MoO_x-based contact, and $j_{0h}^{(n)aSiH}$ and $J_{0e}^{(n)aSiH}$ stand for the hole and electron equilibrium exchange current densities at the (n)a-Si:H-based contact. R_S is an ohmic series resistance which we added to the original equation to account for non-contact related resistive losses (in the MoO_x, ITO, and Ag electrodes). In light of the previous results on shunt resistance, the latter was not considered in the equation. To reproduce the *J-V* curves of samples with various MoO_x-layer thicknesses, we varied J_{0h}^{MoOx}, j_{0e}^{MoOx}, $J_{0e}^{(n)aSiH}$, $j_{0h}^{(n)aSiH}$, and R_S. This modelling thus does not rely on specific materials properties (work functions, barriers height, nature of carrier transport) as inputs. The experimental *J-V* curves and the fitted ones are plotted on Fig. 9.b). The disagreement between experimental and simulated data around the rectifying region of the JV curves for cells from 3-nm to 1-nm-thick MoO_x can tentatively be attributed to micro-shunts which could impact the *FF* [44], [45], strong passivation damages that occurred during the cleaning step, or to the aforementioned screen-printing issue.

$$J(V) = -\left(J_L + j_{0e}^{MoOx} + j_{0h}^{(n)aSiH}\right) + \frac{J_L + j_{0e}^{MoOx} + J_{0e}^{(n)aSiH}}{1 + \frac{J_{0e}^{(n)aSiH}}{j_{0e}^{MoOx}} e^{\frac{-V-R_SJ}{V_T}}} + \frac{J_L + j_{0h}^{(n)aSiH} + J_{0h}^{MoOx}}{1 + \frac{J_{0h}^{MoOx}}{j_{0h}^{(n)aSiH}} e^{\frac{-V-R_SJ}{V_T}}} \quad (1)$$

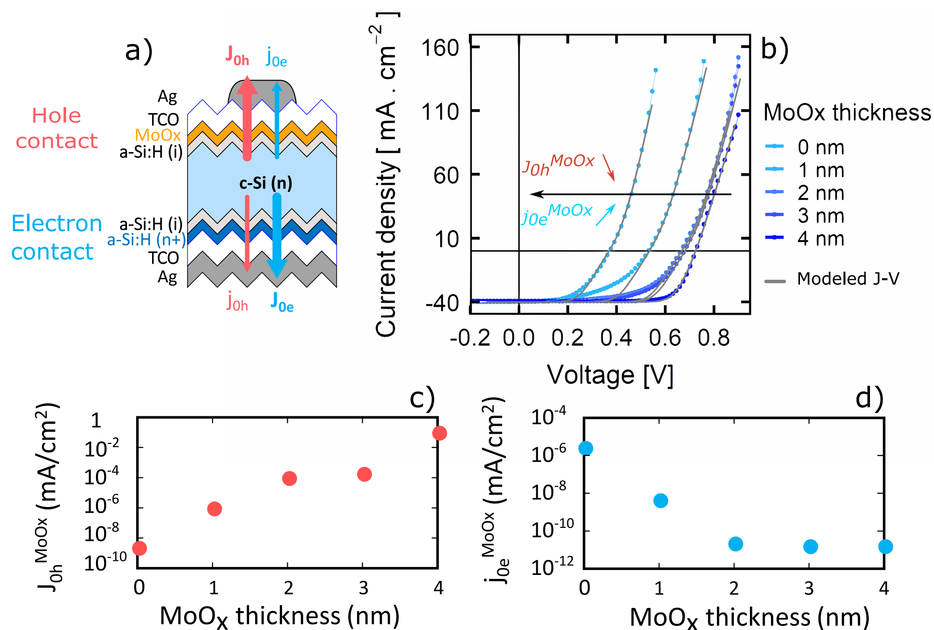

Fig. 9: a) schematic representation of the four different current density involved in Roe *et al.* model; b) *J-V* experimental (shades of blue) curves and their fitted data (shades of yellow); c) and d) evolution of j_{0e}^{MoOx} and J_{0h}^{MoOx} with MoO_x layer thickness.

For all MoO_x thicknesses, $J_{0e}^{(n)aSiH}$ and $j_{0h}^{(n)aSiH}$ barely varied around 10^3 mA/cm² and 1.3×10^{-14} mA/cm² respectively, while J_{0h}^{MoOx} decreased in a quasi-exponential way (see Fig. 9.c)), from 1 mA/cm² to 4×10^{-9} mA/cm², with MoO_x thickness decrease. On the contrary, j_{0e}^{MoOx} increased from 1.8×10^{-11} to 3×10^{-6} mA/cm² for MoO_x below 2 nm.

The shunt resistance was kept constant at 10 kΩ·cm², and the series resistance decreased from 1.3 to 0.85 Ω·cm². Still, we can observe that the selectivity loss is caused by a worsening of both the electron-blocking (j_{0e}^{MoOx} increase) and hole-collecting (J_{0h}^{MoOx} decrease) ability of the contact.

3) *In situ hole contact work function estimation*

A qualitative analysis of band diagrams (Fig. 10) hints that aforesaid loss could come from a reduction of MoO_x work function. Besides, a work function decrease affecting MoO_x was often reported in literature [46], [47], and Greiner *et al.* notably reported that MoO_x work function is diminished near interfaces due to chemical and physical reactions with the substrate material it grows on [48]. Accordingly, under a critical thickness, MoO_x work function is affected over the whole layer. In our case, an oxygen/hydrogen exchange could occur at the (i)a-Si:H/MoO_x interface [46], [49] and provoke MoO_x chemical reduction, decreasing its work function. At the ITO/MoO_x interface, oxygen exchange (thermodynamically possible) or reduction through charge transfer due to work function misalignment could also occur [48].

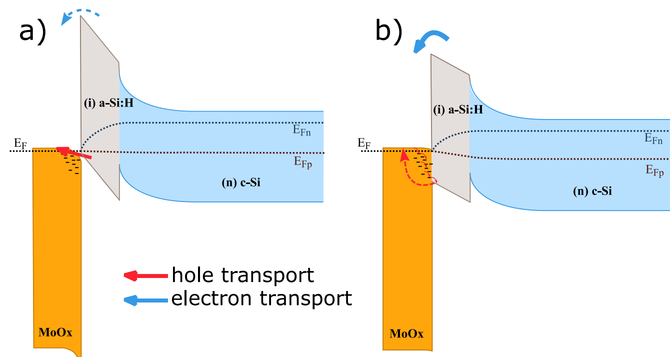

Fig.10: Qualitative band diagram scheme of the hole contact for a MoO_x-based SHJ under illumination and at open circuit, with a) a high work function and b) a low work function. E_{Fn} and E_{Fp} are the quasi Fermi levels for electrons and holes respectively.

Fig. 10 exhibits our MoO_x-based hole contact band diagram, for a MoO_x with a high (a.) and low (b.) work function. We added a simplified carrier transport, schematized by the blue and red arrows. In case of a high work function, hole (red arrow) transfer from the (i)a-Si:H valence band to the MoO_x conduction band is possible through band to band tunneling or trap assisted tunneling [50] (more correctly - but equivalently - electrons coming from ITO and MoO_x recombines with holes at the MoO_x/(i)a-Si:H interface), whereas parasitic electrons (blue arrow) face a high energetic barrier due to band bending. In case of a lower work function, the misalignment between the MoO_x conduction band and the (i)a-Si:H valence band forces transport through trap assisted tunneling which reduces the extraction efficiency. Simultaneously, the energetic barriers preventing electrons to pass is also lowered, enhancing parasitic electron thermionic emission and unintended recombination. This behavior is consistent with the trends observed for carrier density currents extracted from the Roe *et al.* modelling.

In a simple approach, assuming parasitic electrons at hole contact travel through thermionic emission, we can calculate the barrier height φ_b, the energy difference between the Fermi level at the interface with (n)c-Si and the (i)a-Si:H conduction band maximum, thanks to the electron current density j_{0e}^{MoOx} we found with the Roe *et al.* model and using the thermionic emission equation (2) [51]:

$$j_{0e} = A^* T^2 e^{\frac{-\varphi_b}{qV_T}} \quad (2)$$

with $A*$ the effective Richardson constant and T the temperature. With an analysis in temperature from 0 °C to 70

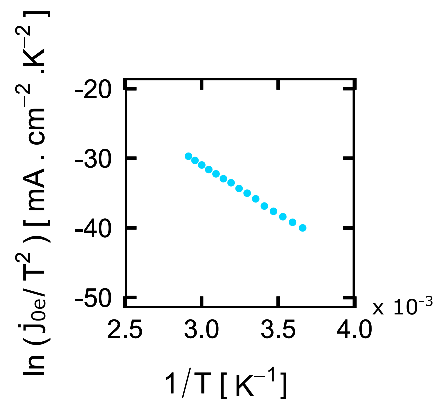

Fig. 11: Plot of $ln(j_{0e}^{MoOx}/T^2)$ as a function of $1/T$, over 0 °C to 70 °C. Linearity of the plot proves the thermionic emission nature of electron transport. The different j_{0e}^{MoOx} were extracted from a MoO_x-based cell experimental *J-V* fitting with Roe *et al.* modeling.

°C, we confirmed that the electron current passing through the hole contact indeed follows this law (see Fig. 11). Following thermionic emission mechanism, decreasing the barrier height

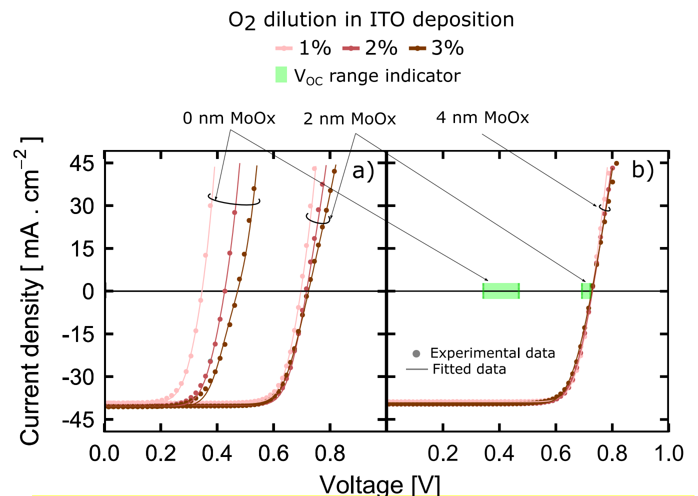

Fig. 12: *J-V* experimental and fitted curves of solar cells with 0 nm, 2 nm and 4 nm of MoO_x, with three different ITO oxygen doping each. For more clarity, solar cells with 0 and 2 nm of MoO_x are plotted on graph a), and 4-nm-MoO_x thick cells are plotted on graph b) with 0-nm and 2-nm V_{OC} range added for comparison.

provokes thermionic current increase. Here, according to Fig. 9.d, parasitic thermionic electron current is increasing with decreasing MoO_x thickness, so the barrier height blocking electrons might indeed reduce - and so is the MoO_x work

function - as MoO_x thickness reduces. We did not model J_{0h}^{MoOx} due to complexity involved in trap or multi-trap assisted tunneling mechanisms, and to the lack of information linking J and the energy barriers in such transport. Yet, fitting of the parasitic electron current can be used to estimate the hole contact work function through calculation of φ_b. Fig. 9.d indicates that above 2 nm of MoO_x, j_{0e}^{MoOx} is plateauing even though J_{0h}^{MoOx} is still variating. This mean that our work function estimation with j_{0e}^{MoOx} will also saturate for MoO_x layers above 2 nm, which might be physically incorrect as J_{0h}^{MoOx} still increases from 2 nm to 4 nm.

To verify this hypothesis, and to get more accurate fitted data to properly estimate hole contact work function, we processed new MoO_x-based solar cells with 0 nm, 2 nm and 4 nm MoO_x layers, each coated with ITOs of three different doping obtained by variating the oxygen dilution in Ar during sputtering deposition. Hall effect measurements gave bulk concentrations of 4.10^{20} cm^{-3}, 1.10^{20} cm^{-3} and 3.10^{19} cm^{-3} for an oxygen dilution of 1%, 2 % and 3 % respectively. Fig. 12 illustrates the obtained J-V curves, with both experimental (symbols) and fitted (lines) data. Compared to the previous series, we observe the same trend for V_{OC}, with lower V_{OC} for thinner MoO_x thickness. Comparing now the influence of ITO doping, there is a strong impact when ITO is directly in contact with (i)aSi:H (0 nm of MoO_x) as it constitutes the selective layer in this case (which is not very selective considering the poor V_{OC}s). As expected, the less doped ITO – so the highest work function one – is the one giving the highest V_{OC}. Applying 2 nm of MoO_x already efficiently screens the ITO influence as the V_{OC} spread is much narrower (Fig. 12.a and b.), and highly enhance selectivity with a V_{OC} gain of around 300 mV compared to the cells with ITO only. With 4 nm of MoO_x, ITO influence seems completely screened and V_{OC} still slightly improved compared to 2-nm-MoO_x-based cells. These results highlight that even though j_{0e}^{MoOx} is similar for 4 nm or 2 nm thick MoO_x, work function of 2 nm MoO_x layer in this contact stack is not high enough to screen the ITO work function mismatch influence on carrier extraction, contrary to a 4 nm MoO_x layer.

With the approach developed in the previous paragraph, we can use thermionic emission law to extract the barrier height, and quantitatively estimate the hole contact work function of this new set of data which match the simulations. For all solar cells, we set $A^* = 70$ A/cm²·K² assuming A^* for a-Si is close to those of c-Si [52], and approximates this value for p-type c-Si [51]. Assuming that the cells work in low to moderate injection under one sun, what is suggested by Suns-V_{OC} measurements, and that there is a Fermi level pinning at the interface MoO_x/(i)a-Si:H, we can suppose that φ_b also represents the barrier height between MoO_x Fermi level and (i)a-Si:H conduction band. Using 3.9 eV for a-Si:H electron affinity (E_A) [53][54], we can extract MoO_x work function (WF), so that: $WF^{MoOx} = \varphi_b + E_A^{aSi:H}$. The calculated work function values range therefore from 4.6 eV to 4.8 for the cells with no MoO_x layer, and around 5 eV for MoO_x layers of 2 nm and 4 nm. The similar work function found for both 2 nm and 4 nm MoO_x originates from the aforementioned limitation of extracting WF through j_{0e}^{MoOx}, but must be different according to results of Fig. 12 experiment. The low values obtained compared to literature (typically around 6.5 eV [23], [48]) suggest that even the thickest investigated MoO_x film is already strongly reduced. This can be expected since it is exposed to air between process steps (work function easily reduced by 1 eV [23], [55] [56]), and is sandwiched between two lower-work function layers prone to oxidation (thermodynamically and electronically [48], [56]), and significant sub-gap absorption is observed optically for a-Si:H/MoO_x/ITO stacks [49]. This low value could also be understood as our calculated WF is an effective WF of the entire hole contact stack ITO/MoO_x/(i)a-Si:H/(n)c-Si (still with MoO_x WF playing a central role in the thermionic emission). Note that in the 0 nm MoO_x case, corresponding to direct contact of (i)a-Si:H with ITO, the obtained values are in agreement with the range of 4.5 eV to 5.1 eV found in literature [57]–[59]. This mid-gap position correlates well with our obtained V_{OC} value around 350 mV (see Fig. 4.a and 12)) and the one found in literature for such TCO work function on n-type c-Si [60], [61], corresponding to the absence of any selectivity at the hole contact. It suggests that this methodology coupling J_{0s} with energy barriers and band diagram theory could be a valuable approach to characterize the work function of electrodes in use within the solar cells contact stack.

V. Conclusion

In this work, we showed that an appreciable short circuit current gain is still possible when decreasing MoO_x thickness from 4 nm to 1 nm, but at the cost of a severe degradation of FF and V_{OC}. The latter is due to both surface passivation and mainly selectivity loss, caused by a too thin protection against ITO sputtering and a probable reduction of the MoO_x work function respectively. Below 1 nm of MoO_x, we also discovered that the J_{SC} value was limited by the strong surface passivation damage. All these results are supported by lifetime, Suns-V_{OC}, and PL measurements, calculations and simulations via PC1D and a model proposed by Roe *et al.* [43]. We experimentally demonstrate that MoO_x optimal thickness appears to be 4 nm, a figure in agreement with Mazzarella *et al* work [62]. We also highlight that the parasitic electron current at the hole contact is not increasing from 4 nm to 2 nm, whereas the majority hole current is decreasing already.

This work overall showed that MoO_x shows limitations to fabricate very-high-efficiency silicon heterojunction solar cells. However, further investigations could still be made, for instance using alternative TCO material (and/or deposition technique), or careful tuning of the passivation material and its interface with MoO_x are particularly relevant routes [62].

Acknowledgment

The authors would like to thank X. Niquille, C. Allebé, and P. Wyss for the wafer cleaning and texturization, N. Badel for the Ag screen-printing metallization, and C. Bucher, N. Fürst and S. Dunand for technical support.

References

[1] D. Adachi, J. L. Hernández, and K. Yamamoto, “Impact of carrier recombination on fill factor for large area heterojunction crystalline silicon solar cell with 25.1% efficiency,” *Appl. Phys. Lett.*, vol. 107, no. 23, p. 233506, Dec. 2015, doi: 10.1063/1.4937224.

[2] K. Yoshikawa *et al.*, “Silicon heterojunction solar cell with interdigitated back contacts for a photoconversion efficiency over

26%," *Nat. Energy*, vol. 2, no. 5, p. 17032, Mar. 2017, doi: 10.1038/nenergy.2017.32.

[3] M. Tanaka *et al.*, "Development of New a-Si/c-Si Heterojunction Solar Cells: ACJ-HIT (Artificially Constructed Junction-Heterojunction with Intrinsic Thin-Layer)," *Jpn. J. Appl. Phys.*, vol. 31, no. Part 1, No. 11, pp. 3518–3522, Nov. 1992, doi: 10.1143/JJAP.31.3518.

[4] H. Fujiwara and M. Kondo, "Effects of a-Si:H layer thicknesses on the performance of a-Si:H∕c-Si heterojunction solar cells," *J. Appl. Phys.*, vol. 101, no. 5, p. 054516, Mar. 2007, doi: 10.1063/1.2559975.

[5] Z. C. Holman *et al.*, "Current Losses at the Front of Silicon Heterounction Solar Cells," *IEEE J. Photovoltaics*, vol. 2, no. No. 1, 2012, doi: 10.1109/JPHOTOV.2011.2174967.

[6] T. Watahiki *et al.*, "Rear-emitter Si heterojunction solar cells with over 23% efficiency," 2015.

[7] Mazzarella *et al.*, "Nanocrystalline n-Type Silicon Oxide Front Contacts for Silicon Heterojunction Solar Cells : Photocurrent Enhancement on Planar and Textured Substrates," vol. 8, no. 1, pp. 70–78, 2018.

[8] L. Mazzarella, S. Kirner, B. Stannowski, L. Korte, B. Rech, and R. Schlatmann, "P-type microcrystalline silicon oxide emitter for silicon heterojunction solar cells allowing current densities above 40 mA/cm2," *Appl. Phys. Lett.*, vol. 106, no. 2, pp. 0–5, 2015, doi: 10.1063/1.4905906.

[9] A. N. Fioretti, M. Boccard, R. Monnard, and C. Ballif, "Low-Temperature p-Type Microcrystalline Silicon as Carrier Selective Contact for Silicon Heterojunction Solar Cells," *IEEE J. Photovoltaics*, vol. 9, no. 5, pp. 1–8, 2019, doi: 10.1109/jphotov.2019.2917550.

[10] M. Kohler *et al.*, "Optimization of Transparent Passivating Contact for Crystalline Silicon Solar Cells," *IEEE J. Photovoltaics*, vol. 10, no. 1, pp. 46–53, 2020, doi: 10.1109/JPHOTOV.2019.2947131.

[11] M. Boccard *et al.*, "Hole-Selective Front Contact Stack Enabling 24.1%-Efficient Silicon Heterojunction Solar Cells," *IEEE J. Photovoltaics*, vol. 11, no. 1, pp. 9–15, 2021, doi: 10.1109/JPHOTOV.2020.3028262.

[12] Z. Yang *et al.*, "Tuning of the Contact Properties for High- E ffi ciency Si/PEDOT:PSS Heterojunction Solar Cells," 2017, doi: 10.1021/acsenergylett.7b00015.

[13] D. Zielke, C. Niehaves, W. Lövenich, A. Elschner, M. Hörteis, and J. Schmidt, "Organic-silicon Solar Cells Exceeding 20% Efficiency," *Energy Procedia*, vol. 77, pp. 331–339, 2015, doi: 10.1016/j.egypro.2015.07.047.

[14] X. Yang, Q. Bi, H. Ali, K. Davis, W. V. Schoenfeld, and K. Weber, "High-Performance TiO2-Based Electron-Selective Contacts for Crystalline Silicon Solar Cells," *Adv. Mater.*, pp. 5891–5897, 2016, doi: 10.1002/adma.201600926.

[15] W. Ji, T. Allen, X. Yang, G. Zeng, S. De Wolf, and A. Javey, "Polymeric Electron-Selective Contact for Efficiency Exceeding 19%," 2020, doi: 10.1021/acsenergylett.0c00110.

[16] J. Bullock *et al.*, "Dopant-Free Partial Rear Contacts Enabling 23% Silicon Solar Cells," *Adv. Energy Mater.*, vol. 9, no. 9, pp. 1–6, 2019, doi: 10.1002/aenm.201803367.

[17] S. Zhong *et al.*, "Mitigating Plasmonic Absorption Losses at Rear Electrodes in High-Efficiency Silicon Solar Cells Using Dopant-Free Contact Stacks," *Adv. Funct. Mater.*, vol. 30, no. 5, 2020, doi: 10.1002/adfm.201907840.

[18] W. Wu *et al.*, "22% efficient dopant-free interdigitated back contact silicon solar cells," in *AIP Conference Proceedings*, 2018, vol. 1999, no. 1, p. 40025.

[19] L. G. Gerling *et al.*, "Transition metal oxides as hole-selective contacts in silicon heterojunctions solar cells," *Sol. Energy Mater. Sol. Cells*, vol. 145, pp. 109–115, 2016, doi: 10.1016/j.solmat.2015.08.028.

[20] H. Imran, T. M. Abdolkader, and N. Z. Butt, "Carrier-Selective NiO / Si and TiO 2 / Si Contacts for," vol. 63, no. 9, pp. 3584–3590, 2016.

[21] V. K. KOMARALA, "Silicon Heterojunction Solar Cell Fabrication Using Nickel Oxide Hole-Selective Contact," 2020, p. EUPVSEC oral presentation (1AO.2.5).

[22] W. Lin, "Dopant-free bifacial silicon solar cells," *Sol. RRL*, vol. Research A, no. Accepted, 2021.

[23] C. Battaglia *et al.*, "Hole Selective MoO," *Nano Lett.*, vol. 14, pp. 967–971, 2014, doi: dx.doi.org/10.1021/nl404389u.

[24] J. Bullock *et al.*, "Stable Dopant-Free Asymmetric Heterocontact Silicon Solar Cells with Efficiencies above 20%," *ACS Energy Lett.*, vol. 3, no. 3, pp. 508–513, Mar. 2018, doi: 10.1021/acsenergylett.7b01279.

[25] M. Bivour, J. Temmler, H. Steinkemper, and M. Hermle, "Molybdenum and tungsten oxide: High work function wide band gap contact materials for hole selective contacts of silicon solar cells," *Sol. Energy Mater. Sol. Cells*, vol. 142, pp. 34–41, Nov. 2015, doi: 10.1016/J.SOLMAT.2015.05.031.

[26] J. Dréon *et al.*, "23.5%-efficient silicon heterojunction silicon solar cell using molybdenum oxide as hole-selective contact," *Nano Energy*, vol. 70, 2020, doi: 10.1016/j.nanoen.2020.104495.

[27] Z. Mrazkova *et al.*, "Optical properties and performance of pyramidal texture silicon heterojunction solar cells: Key role of vertex angles," *Prog. Photovoltaics Res. Appl.*, vol. 26, no. 6, pp. 369–376, 2018, doi: 10.1002/pip.2994.

[28] J. Dréon, Q. Jeangros, J. Cattin, J. Haschke, L. Antognini, and C. Ballif, "Nano Energy 23 . 5 % -efficient silicon heterojunction silicon solar cell using molybdenum oxide as hole-selective contact," vol. 70, no. October 2019, 2020, doi: 10.1016/j.nanoen.2020.104495.

[29] R. A. Sinton, A. Cuevas, and M. Stuckings, "Quasi-steady-state photoconductance, a new method for solar cell material and device characterization," in *Conference Record of the Twenty Fifth IEEE Photovoltaic Specialists Conference - 1996*, 1996, pp. 457–460, doi: 10.1109/PVSC.1996.564042.

[30] R. A. Sinton and A. Cuevas, "Contactless determination of current-voltage characteristics and minority-carrier lifetimes in semiconductors from quasi-steady-state photoconductance data," *Appl. Phys. Lett.*, vol. 69, no. 17, pp. 2510–2512, 1996, doi: 10.1063/1.117723.

[31] S. De Wolf and M. Kondo, "Nature of doped a-Si:H/c-Si interface recombination," *J. Appl. Phys.*, vol. 105, no. 10, 2009, doi: 10.1063/1.3129578.

[32] W. Beyer, J. Herion, and H. Wagner, "Fermi energy dependence of surface desorption and diffusion of hydrogen in a-Si:H," *J. Non. Cryst. Solids*, vol. 114, no. PART 1, pp. 217–219, 1989, doi: 10.1016/0022-3093(89)90117-8.

[33] M. Glatthaar *et al.*, "Evaluating luminescence based voltage images of silicon solar cells," *J. Appl. Phys.*, vol. 108, no. 1, pp. 1–5, 2010, doi: 10.1063/1.3443438.

[34] C. Shen, H. Kampwerth, M. Green, T. Trupke, J. Carstensen, and A. Schütt, "Spatially resolved photoluminescence imaging of essential silicon solar cell parameters and comparison with CELLO measurements," *Sol. Energy Mater. Sol. Cells*, vol. 109, pp. 77–81, 2013, doi: 10.1016/j.solmat.2012.10.010.

[35] M. Bivour *et al.*, "Doped Layer Optimization for Silicon Heterojunctions by Injection-Level-Dependent Open-Circuit Voltage Measurements," vol. 4, no. 2, pp. 566–574, 2014.

[36] R. Sinton and A. Cuevas, "A quasi-steady-state open-circuit voltage method for solar cell characterization," *16th Eur. Photovolt. Sol. …*, no. May, pp. 1–4, 2000, doi: citeulike-article-id:6901946.

[37] S. W. Glunz, J. Nekarda, H. Mäckel, and A. Cuevas, "ANALYZING BACK CONTACTS OF SILICON SOLAR CELLS BY SUNS-VOC-MEASUREMENTS AT HIGH ILLUMINATION DENSITIES," no. September, 2007.

[38] S. M. Sze, "Physics of Semiconductor Devices," *Electronics and Power*, vol. 16, no. 1. p. 811, 1969, doi: 10.1049/ep.1970.0039.

[39] T. Kirchartz, F. Deledalle, P. S. Tuladhar, J. R. Durrant, and J. Nelson, "On the differences between dark and light ideality factor in polymer:Fullerene solar cells," *J. Phys. Chem. Lett.*, vol. 4, no. 14, pp. 2371–2376, 2013, doi: 10.1021/jz4012146.

[40] M. Green, "Limits on the Open-circuit Voltage and Efficiency of Silicon Solar Cells Imposed by Intrinsic Auger Processes," *IEEE Trans. Electron Devices*, vol. d, 1984.

[41] K. R. McIntosh, P. P. Altermatt, and G. Heiser, "Depletion-Region Recombination in Silicon Solar Cells: When Does mdr = 2?," *16th Eur. Photovolt. Sol. Energy Conf.*, no. May, pp. 250–253, 2000.

[42] J. Cattin, "Characterisation of Silicon Heterojunction Solar Cells Beyond Standard Test Conditions," EPFL, 2019.

[43] E. T. Roe, K. E. Egelhofer, and M. C. Lonergan, "Exchange current density model for the contact-determined current-voltage behavior of solar cells," *J. Appl. Phys.*, vol. 125, no. 22, 2019, doi: 10.1063/1.5090519.

[44] J. Cattin, M. Boccard, and C. Ballif, "Characterization of silicon

heterojunction solar cells beyond standard test conditions," 2020.

[45] K. Mcintosh and K. R. Mcintosh, "Lumps, Humps and Bumps: Three Detrimental Effects in the Current–Voltage Curve of Silicon Solar Cells," no. September, 2017, doi: 10.13140/RG.2.2.19197.26083.

[46] S. Essig *et al.*, "Toward Annealing-Stable Molybdenum-Oxide-Based Hole-Selective Contacts For Silicon Photovoltaics," *Sol. RRL*, vol. 2, no. 4, p. 1700227, Apr. 2018, doi: 10.1002/solr.201700227.

[47] C. Messmer, M. Bivour, J. Schön, S. W. Glunz, and M. Hermle, "Numerical Simulation of Silicon Heterojunction Solar Cells Featuring Metal Oxides as Carrier-Selective Contacts," *IEEE J. PHOTOVOLTAICS*, vol. 1, doi: 10.1109/JPHOTOV.2018.2793762.

[48] M. T. Greiner, L. Chai, M. G. Helander, W. Tang, and Z. Lu, "Metal / Metal-Oxide Interfaces : How Metal Contacts Affect the Work Function and Band Structure of MoO 3," pp. 215–226, 2013, doi: 10.1002/adfm.201200993.

[49] D. Sacchetto *et al.*, "ITO/MoOx/a-Si:H(i) Hole-Selective Contacts for Silicon Heterojunction Solar Cells: Degradation Mechanisms and Cell Integration," *IEEE J. Photovoltaics*, vol. 7, no. 6, pp. 1584–1590, 2017, doi: 10.1109/JPHOTOV.2017.2756066.

[50] D. Scirè, P. Procel, A. Gulino, O. Isabella, M. Zeman, and I. Crupi, "Sub-gap defect density characterization of molybdenum oxide: An annealing study for solar cell applications," *Nano Res.*, vol. 13, no. 12, pp. 3416–3424, Dec. 2020, doi: 10.1007/s12274-020-3029-9.

[51] S. M. Sze and K. N. Kwok, *Physics of Semiconductor Devices Physics of Semiconductor Devices*, vol. 10. 1995.

[52] A. Deneuville and M. H. Brodsky, "Influence of preparation conditions on forward-bias currents of amorphous silicon Schottky diodes," *J. Appl. Phys.*, vol. 50, no. 3, pp. 1414–1421, 1979, doi: 10.1063/1.326124.

[53] M. Schmidt *et al.*, "Physical aspects of a-Si:H/c-Si hetero-junction solar cells," *Thin Solid Films*, vol. 515, no. 19 SPEC. ISS., pp. 7475–7480, 2007, doi: 10.1016/j.tsf.2006.11.087.

[54] J. P. Kleider, A. S. Gudovskikh, and P. Roca I Cabarrocas, "Determination of the conduction band offset between hydrogenated amorphous silicon and crystalline silicon from surface inversion layer conductance measurements," *Appl. Phys. Lett.*, vol. 92, no. 16, 2008, doi: 10.1063/1.2907695.

[55] J. Meyer and A. L. Kahn, "Electronic structure of molybdenum-oxide films and associated charge injection mechanisms in organic devices," *J. Photonics Energy*, vol. 1, no. 1, p. 011109, Jan. 2011, doi: 10.1117/1.3555081.

[56] L. G. Gerling, C. Voz, R. Alcubilla, and J. Puigdollers, "Origin of passivation in hole-selective transition metal oxides for crystalline silicon heterojunction solar cells," *J. Mater. Res.*, vol. 32, no. 2, pp. 260–268, 2017, doi: 10.1557/jmr.2016.453.

[57] E. Centurioni and D. Iencinella, "Role of front contact work function on amorphous silicon/crystalline silicon heterojunction solar cell performance," *IEEE Electron Device Lett.*, vol. 24, no. 3, pp. 177–179, 2003, doi: 10.1109/LED.2003.811405.

[58] J. S. Kim *et al.*, "Kelvin probe and ultraviolet photoemission measurements of indium tin oxide work function: a comparison," *Synth. Met.*, vol. 111, pp. 311–314, 2000, doi: 10.1016/S0379-6779(99)00354-9.

[59] K. Sugiyama, H. Ishii, Y. Ouchi, and K. Seki, "Dependence of indium-tin-oxide work function on surface cleaning method as studied by ultraviolet and x-ray photoemission spectroscopies," *J. Appl. Phys.*, vol. 87, no. 1, pp. 295–298, 2000, doi: 10.1063/1.371859.

[60] M. Bivour, C. Reichel, M. Hermle, and S. W. Glunz, "Improving the a-Si:H(p) rear emitter contact of n-type silicon solar cells," *Sol. Energy Mater. Sol. Cells*, vol. 106, pp. 11–16, 2012, doi: 10.1016/j.solmat.2012.06.036.

[61] K. U. Ritzau *et al.*, "TCO work function related transport losses at the a-Si:H/TCO-contact in SHJ solar cells," *Sol. Energy Mater. Sol. Cells*, vol. 131, pp. 9–13, 2014, doi: 10.1016/j.solmat.2014.06.026.

[62] L. Mazzarella *et al.*, "Interface Treatment to Improve the (I)a-Si:H/MoOx Stack for Passivating Contact Solar Cells," *Present. EUPVSEC Conf.*, 2020.